Gravitational form factors and mechanical properties of proton in a light-front quark-diquark model

Dipankar Chakrabarti[1,*] Chandan Mondal[2,3,4,†] Asmita Mukherjee,[5,‡] Sreeraj Nair[2,3,4,§] and Xingbo Zhao[2,3,4,‖]

[1]*Department of Physics, Indian Institute of Technology Kanpur, Kanpur 208016, India*
[2]*Institute of Modern Physics, Chinese Academy of Sciences, Lanzhou 730000, China*
[3]*School of Nuclear Science and Technology, University of Chinese Academy of Sciences, Beijing 100049, China*
[4]*CAS Key Laboratory of High Precision Nuclear Spectroscopy, Institute of Modern Physics, Chinese Academy of Sciences, Lanzhou 730000, China*
[5]*Department of Physics, Indian Institute of Technology Bombay, Powai, Mumbai 400076, India*

We obtain the gravitational form factors (GFFs) and investigate their applications for the description of the mechanical properties, i.e., the distributions of pressures, shear forces inside proton, and the mechanical radius, in a light-front quark-diquark model constructed by the soft-wall AdS/QCD. The GFFs, $A(Q^2)$ and $B(Q^2)$ are found to be consistent with the lattice QCD, while the qualitative behavior of the D-term form factor is in agreement with the extracted data from the deeply virtual Compton scattering (DVCS) experiments at JLab, the lattice QCD, and the predictions of different phenomenological models. The pressure and shear force distributions are also consistent with the results of different models.

I. INTRODUCTION

The mechanical properties of the nucleon, namely how the mass, spin and pressure are distributed among the quarks and gluons inside the nucleon is a topic of intense interest in recent days [1–26]. These information are related to the gravitomagnetic form factors, which are expressed as the matrix elements of the energy-momentum tensor in the proton state. The components of the energy-momentum tensor give how matter couples to the gravitational field. Thus these form factors can be obtained by direct measurement of the interaction of the proton with a strong gravitational field, for example, a neutron star. An indirect way to obtain information on them is from hard exclusive processes for example deeply virtual Compton scattering (DVCS) that is sensitive to the gravitational form factors (GFFs) through generalized parton distributions (GPDs) [3]. The GFFs are functions of $t = -Q^2$, which is the squared momentum transfer from the initial to final proton

in DVCS experiment. The GFFs $A(Q^2)$ and $B(Q^2)$ are related to the mass and spin of the proton. The Ji's sum [27] rule relates the second Mellin's moment of the GPDs H and E to the quark contribution to the angular momentum J. First experimental results relevant for the extraction of GPDs were provided by HERA [28–31], HERMES [32], COMPASS [33], and JLab [34,35]. These are also being investigated at JLab 12 GeV upgrade and COMPASS at CERN, and will be accessed at the future electron-ion collider (EIC) [36].

The GFFs A and B are related to the generators of the Poincaré group, which gives constraints on them at zero momentum transfer, that helps in the extraction of these form factors from the experimental data. In contrast the GFF $C(Q^2)$ (also called the D-term) is unconstrained at zero momentum transfer. This form factor is related to the internal properties of the nucleon like the pressure and stress distribution [1,2]. This form factor contributes to the DVCS process when the skewness ξ is nonzero, or when there is nonzero momentum transfer in the longitudinal direction. C form factor has been calculated in several models in the literature. It depends on the correlations between the quarks and gluons in the nucleon. The GFFs of the nucleon have been investigated in the framework of lattice QCD [14,15,37–40], chiral perturbation theory (χPT) [41–43], Skyrme model [10,11], chiral quark soliton model (χQSM) [7,44–47], light-cone QCD sum rules at leading order (LCSR-LO) [4], dispersion relation (DR) [16], instanton picture (IP) [17], and instant and

*dipankar@iitk.ac.in
†mondal@impcas.ac.cn
‡asmita@phy.iitb.ac.in
§sreeraj@impcas.ac.cn
‖xbzhao@impcas.ac.cn

front form (IFF) [2], while the asymptotic behavior of the GFFs has been discussed in Refs. [24,25]. The *D*-term of a free spinless boson is −1 whereas for a free fermion it is zero [1]. In fact for an interacting system, stability requires that the form factor *C* is negative. This form factor has been calculated in MIT bag model [21]. It has also been extracted from JLab data [3]. The bag model underestimates the data while the Skyrme model overestimates it. On the other hand predictions from dispersion relation and χQSM are more close to the data. Renewed interest in the form factor $C(Q^2)$ was generated after a recent result from JLab showed that the pressure distribution is repulsive at the center of the nucleon and confining towards the outer region [3,12]. At the center, it exceeds the pressure estimated for the most dense object in the universe that are the neutron stars. The anisotropy of highly dense nuclear matter has been investigated in the literature. This depends on the interaction of nuclear matter inside neutron stars and cannot be explained by the equation of state (see Ref. [2] and the references therein). Thus the study of the anisotropic pressure distribution inside the nucleon through the GPDs provides an indirect way to investigate such properties in highly dense astronomical objects [22]. Initial theoretical studies of the pressure distribution have been formulated in the Breit frame. The distributions defined in this frame are subject to relativistic corrections. In [2], the pressure and energy distributions inside a nucleon are defined in different frames, including the Breit frame and infinite momentum frame or light-front formalism. The latter has the advantage that because of the fact that transverse boosts are Galilean in light-front framework, one can obtain a relativistic description of the form factors in terms of the light-front wave functions. In Ref. [2], the energy and pressure distributions are investigated by assuming a simple multipole model for the GFFs. In this work we use a quark-diquark model based on AdS/QCD to calculate the GFFs as well as the pressure distributions and compare with other model results in the literature. The light-front wave functions in this model are constructed from the two particle effective wave functions obtained in soft-wall of AdS/QCD [48,49]. This model is consistent with DrellYanWest relation [50] and has been successfully applied to describe many interesting properties of nucleon e.g., electromagnetic form factor, parton distribution functions, GPDs, transverse momentum dependent parton distribution functions, Wigner distributions, transverse densities, etc. [50–58].

The paper is organized as follows. In Sec. II, we give brief introductions to the nucleon LFWFs of the quark-diquark model. The GFFs of proton have been evaluated in this model and discussed in Sec. III. We study the mechanical properties of proton, e.g., the pressures, energy density distributions, shear forces, and the mechanical radius in Sec. IV. Summary is given in Sec. V.

II. LIGHT-FRONT QUARK-DIQUARK MODEL

Here we adopt the generic ansatz for the light-front quark-diquark model for the nucleons [50] where the light-front wave functions are modeled from the solution of soft-wall AdS/QCD. In this model, one contemplates the three valence quarks of the nucleons as an effective system composed of a quark (fermion) and a composite state of diquark (boson), where the spin of the diquark is assumed to be zero (scalar) only. Then the 2-particle Fock-state expansion for proton spin components, $J^z = \pm\frac{1}{2}$ in a frame where the transverse momentum of proton vanishes, i.e., $P \equiv (P^+, \mathbf{0}_\perp, \frac{M^2}{P^+})$, is written as

$$|P; \uparrow(\downarrow)\rangle = \sum_q \int \frac{dx d^2\mathbf{k}_\perp}{2(2\pi)^3\sqrt{x(1-x)}}$$
$$\times \left[\psi_{+q}^{\uparrow(\downarrow)}(x, \mathbf{k}_\perp) \left| +\frac{1}{2}, 0; xP^+, \mathbf{k}_\perp \right\rangle \right.$$
$$\left. + \psi_{-q}^{\uparrow(\downarrow)}(x, \mathbf{k}_\perp) \left| -\frac{1}{2}, 0; xP^+, \mathbf{k}_\perp \right\rangle \right]. \quad (1)$$

However, for nonzero transverse momentum of proton, i.e., $\mathbf{P}_\perp \neq 0$, the physical transverse momenta of quark and diquark are $\mathbf{p}_\perp^q = x\mathbf{P}_\perp + \mathbf{k}_\perp$ and $\mathbf{p}_\perp^D = (1-x)\mathbf{P}_\perp - \mathbf{k}_\perp$, respectively, where $\mathbf{k}_\perp$ represents the relative transverse momentum of the constituents. $\psi_{\lambda_q}^{\lambda_N}(x, \mathbf{k}_\perp)$ are the light-front wave functions with nucleon helicities $\lambda_N = \uparrow(\downarrow)$ and for quark $\lambda_q = \pm$; plus and minus correspond to $+\frac{1}{2}$ and $-\frac{1}{2}$, respectively. The light-front wave functions (LFWFs) at an initial scale $\mu_0^2 = 0.32$ GeV^2 are given by

$$\psi_{+q}^\uparrow(x, \mathbf{k}_\perp) = \varphi_q^{(1)}(x, \mathbf{k}_\perp),$$
$$\psi_{-q}^\uparrow(x, \mathbf{k}_\perp) = -\frac{k^1 + ik^2}{xM}\varphi_q^{(2)}(x, \mathbf{k}_\perp),$$
$$\psi_{+q}^\downarrow(x, \mathbf{k}_\perp) = \frac{k^1 - ik^2}{xM}\varphi_q^{(2)}(x, \mathbf{k}_\perp),$$
$$\psi_{-q}^\downarrow(x, \mathbf{k}_\perp) = \varphi_q^{(1)}(x, \mathbf{k}_\perp), \quad (2)$$

where the wave functions $\varphi_q^{(i=1,2)}(x, \mathbf{k}_\perp)$ are the modified form of the soft-wall AdS/QCD prediction constructed by introducing the parameters $a_q^{(i)}$ and $b_q^{(i)}$ for quark q [49,50],

$$\varphi_q^{(i)}(x, \mathbf{k}_\perp) = N_q^{(i)} \frac{4\pi}{\kappa} \sqrt{\frac{\log(1/x)}{1-x}} x^{a_q^{(i)}} (1-x)^{b_q^{(i)}}$$
$$\times \exp\left[-\frac{\mathbf{k}_\perp^2}{2\kappa^2}\frac{\log(1/x)}{(1-x)^2}\right]. \quad (3)$$

$\varphi_q^{(i)}(x, \mathbf{k}_\perp)$ reduces to the original AdS/QCD solution when $a_q^{(i)} = b_q^{(i)} = 0$ [49]. It should be mentioned here that the modification of the soft-wall AdS/QCD prediction in

Eq. (3) is not unique, while a generic reparametrization function $w(x)$, which unifies the description of polarized and unpolarized quark distributions in the proton, has been introduced in Refs. [59,60]. In this work, we take the AdS/QCD scale parameter $\kappa = 0.4$ GeV, obtained by fitting the nucleon form factors in the soft-wall model of AdS/QCD [61,62]. The quarks are assumed to be massless and the parameters $a_q^{(i)}$ and $b_q^{(i)}$ with the constants $N_q^{(i)}$ are obtained by fitting the electromagnetic properties of the nucleons: $F_1^q(0) = n_q$ and $F_2^q(0) = \kappa_q$, where $n_u = 2$ and $n_d = 1$, the number of valence u and d quarks in proton and the anomalous magnetic moments for the u and d quarks are $\kappa_u = 1.673$ and $\kappa_d = -2.033$ [51,52]. Since no isospin or flavor symmetry is imposed, the parameters for u and d quarks in the model are different. The parameters are given by $a_u^{(1)} = 0.020, a_d^{(1)} = 0.10,$ $b_u^{(1)} = 0.022, b_d^{(1)} = 0.38, a_u^{(2)} = 1.033, a_d^{(2)} = 1.087, b_u^{(2)} = -0.15, b_d^{(2)} = -0.20, N_u^{(1)} = 2.055, N_d^{(1)} = 1.7618, N_u^{(2)} = 1.322, N_d^{(2)} = -2.4827$, and the quarks are assumed to be massless. We estimate a 2% uncertainty in the model parameters. The model inspired by soft-wall AdS/QCD has been extensively used to investigate and reproduce many interesting properties of the nucleons [50–58].

III. GRAVITATIONAL FORM FACTORS

The matrix elements of local operators like electromagnetic current and energy momentum tensor have exact representation in light-front Fock state wave functions of bound states such as hadrons. The gravitational form factors (GFFs) are related to the matrix elements of the energy-momentum tensor, $T^{\mu\nu}$, while the second moment of the GPDs also provides the GFFs. For a spin 1/2 target, the standard parametrization of $T^{\mu\nu}$ involving the GFFs reads [63,64]

$$\langle P', S' | T_i^{\mu\nu}(0) | P, S \rangle$$

$$= \bar{U}(P', S') \left[-B_i(q^2) \frac{\bar{P}^\mu \bar{P}^\nu}{M} + (A_i(q^2) \right.$$

$$+ B_i(q^2)) \frac{1}{2} (\gamma^\mu \bar{P}^\nu + \gamma^\nu \bar{P}^\mu)$$

$$\left. + C_i(q^2) \frac{q^\mu q^\nu - q^2 g^{\mu\nu}}{M} + \bar{C}_i(q^2) M g^{\mu\nu} \right] U(P, S), \quad (4)$$

where $\bar{P}^\mu = \frac{1}{2}(P' + P)^\mu$, $q^\mu = (P' - P)^\mu$, $U(P, S)$ is the spinor, and M is the system mass. In the Drell-Yan frame with $q^+ = 0$, the light-front four momenta are defined as:

$$P = (P^+, P_\perp, P^-) = \left(P^+, 0, \frac{M^2}{P^+} \right),$$

$$P' = (P'^+, P'_\perp, P'^-) = \left(P^+, q_\perp, \frac{q_\perp^2 + M^2}{P^+} \right),$$

$$q = P' - P = \left(0, q_\perp, \frac{q_\perp^2}{P^+} \right). \quad (5)$$

By calculating the $(++)$ component of energy-momentum tensor, one can obtain

$$\langle P + q, \uparrow | T_i^{++}(0) | P, \uparrow \rangle = 2(P^+)^2 A_i(Q^2), \quad (6)$$

$$\langle P + q, \uparrow | T_i^{++}(0) | P, \downarrow \rangle = -2(P^+)^2 \frac{(q_\perp^1 - iq_\perp^2)}{2M} B_i(Q^2), \quad (7)$$

with $Q^2 = -q^2 = \vec{q}_\perp^2$. $A_i(Q^2)$ and $B_i(Q^2)$ are very similar to the Dirac and Pauli form factors which are obtained from the helicity nonflip and helicity flip matrix elements of the vector current. Meanwhile, the form factors $C_i(Q^2)$ and $\bar{C}_i(Q^2)$ can be extracted from the helicity flip matrix elements of $T^{-\perp}$ and T^{+-} components. The matrix elements of $T^{-\perp}$ and T^{+-} give:

$$\langle P + q, \uparrow | T_i^{-2}(0) | P, \downarrow \rangle + \langle P + q, \downarrow | T_i^{-2}(0) | P, \uparrow \rangle$$

$$= \frac{1}{P^+} [2A_i(Q^2)M^2 - (B_i(Q^2) - 4C_i(Q^2))Q^2] \frac{-i(q_\perp^2)^2}{2M}, \quad (8)$$

$$\langle P + q, \uparrow | T_i^{+-}(0) | P, \downarrow \rangle + \langle P + q, \downarrow | T_i^{+-}(0) | P, \uparrow \rangle$$

$$= \left[A_i(Q^2)(2M) - B_i(Q^2) \frac{Q^2}{M} + C_i(Q^2) \frac{4Q^2}{M} \right.$$

$$\left. + \bar{C}_i(Q^2)(4M) \right] (-iq_\perp^2). \quad (9)$$

We consider the energy momentum tensor of a free quark inside the proton to evaluate the form factors:

$$T^{\mu\nu} = \frac{i}{2} [\bar{\psi} \gamma^\mu (\vec{\partial}^\nu \psi) - \bar{\psi} \gamma^\mu \overleftarrow{\partial}^\nu \psi], \quad (10)$$

where ψ is the quark field. Using the two particle Fock states, Eq. (1), and the LFWFs given in Eq. (2), we evaluate

the matrix elements of T^{++}, $T^{-\perp}$, and T^{+-}, and extract the GFFs $A(Q^2)$, $B(Q^2)$, $C(Q^2)$, and $\bar{C}(Q^2)$ from Eqs. (6)–(9). We obtain

$$A^q(Q^2) = \mathcal{I}_1^q(Q^2), \qquad (11)$$

$$B^q(Q^2) = \mathcal{I}_2^q(Q^2), \qquad (12)$$

$$C^q(Q^2) = -\frac{1}{4Q^2}[2M^2\mathcal{I}_1^q(Q^2) - Q^2\mathcal{I}_2^q(Q^2) - \mathcal{I}_3^q(Q^2)], \qquad (13)$$

$$\bar{C}^q(Q^2) = -\frac{1}{4M^2}[\mathcal{I}_3^q(Q^2) - \mathcal{I}_4^q(Q^2)], \qquad (14)$$

where the explicit expressions of the structure integrals $\mathcal{I}_i^q(Q^2)$ are given by

$$\mathcal{I}_1^q(Q^2) = \int dx\, x \left[N_1^2 x^{2a_1}(1-x)^{2b_1+1} + N_2^2 x^{2a_2-2}(1-x)^{2b_2+3} \frac{1}{M^2}\left(\frac{\kappa^2}{\log(1/x)} - \frac{Q^2}{4}\right)\right] \exp\left[-\frac{\log(1/x)}{\kappa^2}\frac{Q^2}{4}\right], \qquad (15)$$

$$\mathcal{I}_2^q(Q^2) = 2\int dx\, N_1 N_2 x^{a_1+a_2}(1-x)^{b_1+b_2+2} \exp\left[-\frac{\log(1/x)}{\kappa^2}\frac{Q^2}{4}\right], \qquad (16)$$

$$\mathcal{I}_3^q(Q^2) = 2\int dx\, N_2 N_1 x^{a_1+a_2-2}(1-x)^{b_1+b_2+2}\left[\frac{4(1-x)^2\kappa^2}{\log(1/x)} + Q^2(1-x)^2 - 4m^2\right] \exp\left[-\frac{\log(1/x)}{\kappa^2}\frac{Q^2}{4}\right], \qquad (17)$$

$$\mathcal{I}_4^q(Q^2) = -2\int dx\, N_2 N_1 x^{a_1+a_2-2}(1-x)^{b_1+b_2+2}\left[\frac{\kappa^2(1-x)^2}{\log(1/x)} + \frac{Q^2(1-x)^2}{4} + m^2\right] \exp\left[-\frac{\log(1/x)}{\kappa^2}\frac{Q^2}{4}\right]. \qquad (18)$$

The expressions of $\mathcal{I}_i^q(Q^2)$ in terms of the overlap of the LFWFs are listed in the Appendix. Although the GFFs $A(Q^2)$ and $B(Q^2)$ are well defined for all regions of Q^2 in our model, it can be noticed from Eq. (13) that the form factor $C(Q^2)$ is not well defined at $Q^2 = 0$. Thus, it is not reachable for the region of small Q^2. We observe that the partial cancellation between $2M^2\mathcal{I}_1^q(Q^2)$ and $\mathcal{I}_3^q(Q^2)$ in Eq. (13) provides a nonzero constant [coefficient of $(Q^2)^0$], which brings the $1/Q^2$ singularity in the form factor $C(Q^2)$. Since, the GFFs are physical observables and therefore finite, we emphasize that the singularity appearing in Eq. (13) is a shortcoming of the actual holographic model used in this work but not an artifact of the light-front framework. However, following the approach adopted in Ref. [4], we approximately fit this form factor in the large $Q^2 (\geq 0.1~\text{GeV}^2)$ region and then employ an analytical continuation of our result to $0 \leq Q^2 < 0.1~\text{GeV}^2$ domain.
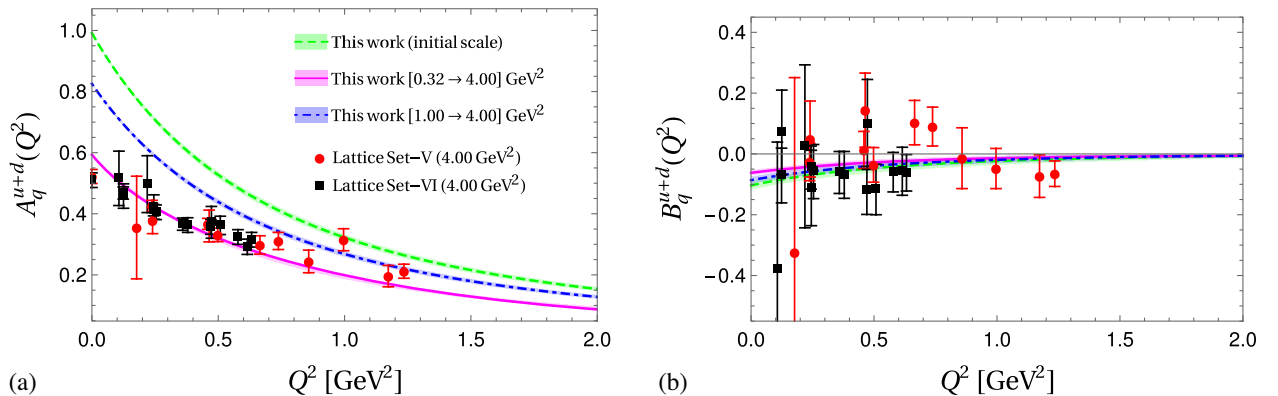

FIG. 1.   The plots of GFFs (a) $A^{u+d}(Q^2)$, and (b) $B^{u+d}(Q^2)$ as functions of Q^2. The dashed green lines with green bands are the results at the initial scale, while the solid magenta lines with magenta bands and the dash-dotted blue lines with purple bands represent the results at $\mu^2 = 4~\text{GeV}^2$ evolved from the initial scales $\mu_0^2 = 0.32~\text{GeV}^2$ and $\mu_0^2 = 1.00~\text{GeV}^2$, respectively. The error bands correspond to 2% uncertainty in the model parameters. Our results are compared with the lattice results (red circle and black square) at scale $\mu^2 = 4~\text{GeV}^2$ [38].
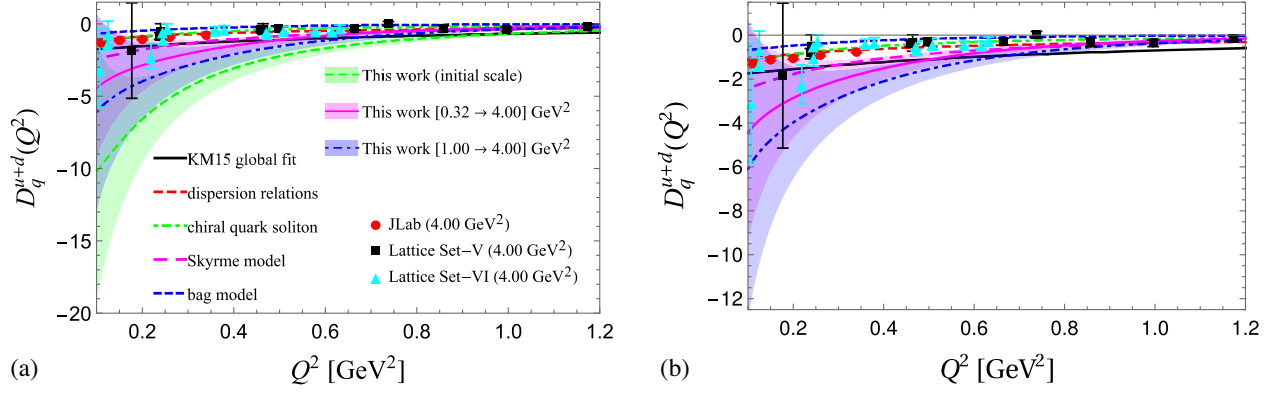
FIG. 2. The plots of GFF $D_q^{u+d}(Q^2) = 4C_q^{u+d}(Q^2)$ as a function of Q^2. The dashed green line with green band, the solid magenta line with magenta band, and the dash-dotted blue line with purple band in plot (a) represent the results at the initial scale and at scale $\mu^2 = 4$ GeV^2 evolved from the initial scales $\mu_0^2 = 0.32$ GeV^2 and $\mu_0^2 = 1.00$ GeV^2, respectively. We show the result at $\mu^2 = 4$ GeV^2 evolved from $\mu_0^2 = 0.32$ GeV^2 and $\mu_0^2 = 1.00$ GeV^2 separately in plot (b). The error bands correspond to 2% uncertainty in the model parameters. The red circles are the experimental data from the Jefferson Lab [3] and the cyan triangles and black squares correspond to the lattice results [38]. Our results are compared with KM15 global fit [23] (solid black), dispersion relations [16] (dashed red), chiral quark soliton [7] (dash-dotted green), Skyrme model [10] (big dashed magenta), and bag model [26] (dashed blue).

Similar to the electromagnetic densities, one can interpret the two-dimensional Fourier transform of the GFF $A(Q^2)$ as the longitudinal momentum density in the transverse plane [6,53,57,65–69], while the GFF $B(Q^2)$ provides an anomalous contribution to the longitudinal momentum densities in a transversely polarized target. In Fig. 1, we show the GFFs $A^{u+d}(Q^2)$ and $B^{u+d}(Q^2)$. Our results are compared with the lattice QCD prediction [38]. Lattice data are available at the scale $\mu^2 = 4$ GeV^2. Thus, in order to compare with lattice QCD prediction, we obtain $A^q(Q^2)$ and $B^q(Q^2)$ at the relevant scale by performing the QCD evolution of the integrands of Eqs. (15) and (16), which represent GPDs $xH^q(x, Q^2)$ and $xE^q(x, Q^2)$,
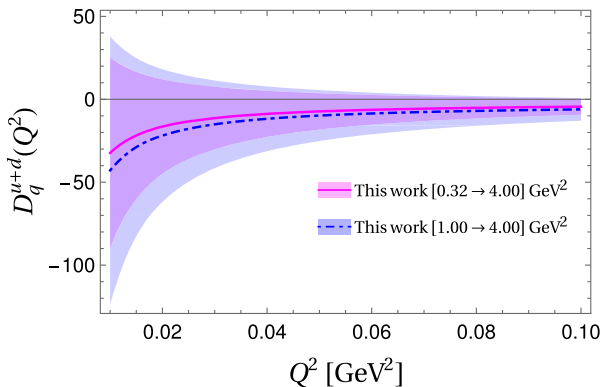
respectively. We adopt the Dokshitzer-Gribov-Lipatov-Altarelli-Parisi (DGLAP) equations [70–72] of QCD with next-to-next-to-leading order for the scale evolution. Explicitly, we evolve the GPDs from the model's scale $\mu_0^2 = 0.32$ GeV^2 to the relevant lattice scale $\mu^2 = 4$ GeV^2 using the higher order perturbative parton evolution toolkit (HOPPET) [73]. We find that after QCD evolution, $A^{u+d}(Q^2)$ and $B^{u+d}(Q^2)$ are consistent with the lattice QCD results. We also choose a higher initial scale $\mu_0^2 = 1.0$ GeV^2 and perform the analysis of our results. We observe that the lower initial scale is preferable after comparing our results with the lattice QCD predictions.

The form factor $4C^{u+d}(Q^2)$, also known as D-term is displayed in Fig. 2, where after scale evolution, we find that the qualitative behavior of our result is compatible with lattice [38] and the experimental data from JLab [3] as well as other theoretical predictions from the KM15 global fit [23], dispersion relation [16], χQSM [7], Skyrme model [10], and bag model [26]. The error

FIG. 3. The plot of GFF $D_q^{u+d}(Q^2) = 4C_q^{u+d}(Q^2)$ at low Q^2 region. The solid magenta lines with magenta bands and the dash-dotted blue lines with purple bands represent the results at $\mu^2 = 4$ GeV^2 evolved from the initial scales $\mu_0^2 = 0.32$ GeV^2 and $\mu_0^2 = 1.00$ GeV^2, respectively. The error bands correspond to 2% uncertainty in the model parameters.

TABLE I. Parameters for the fitted function D_{fit}^q given in Eq. (19) at high Q^2. D_0^{fit} is the distribution at the initial scale, while D_1^{fit} and D_2^{fit} are the distributions at the scale $\mu^2 = 4$ GeV^2 evolved from the initial scale $\mu_0^2 = 0.32$ GeV^2 and $\mu_0^2 = 1.00$ GeV^2, respectively. Here, $[\mu_0^2 \rightarrow \mu^2]$ represents the evolution from μ_0^2 to μ^2.

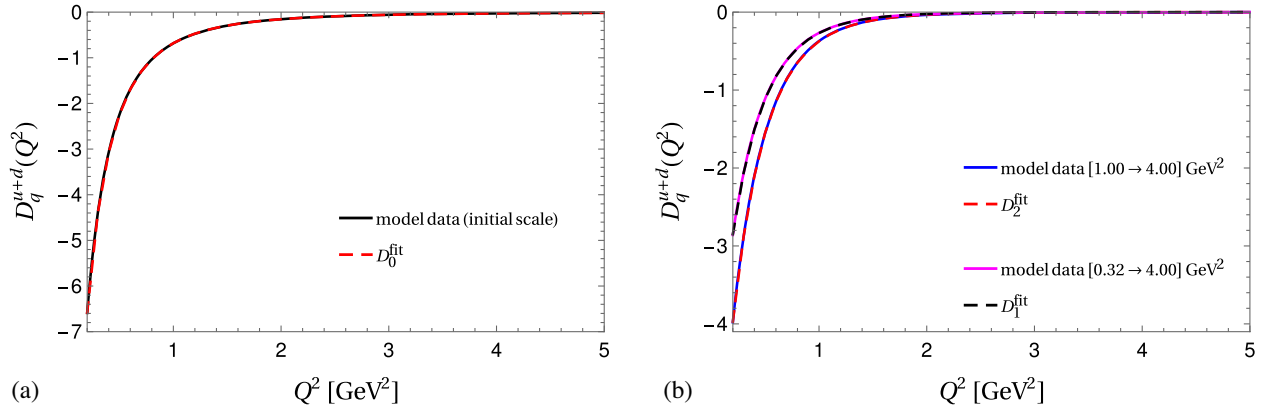| Parameters	μ^2 (GeV^2)	a_q	b_q	c_q
D_0^{fit}	Initial scale	−18.8359	−2.2823	2.7951
D_1^{fit}	[0.32 → 4]	−5.5861	−0.29724	11.6641
D_2^{fit}	[1.00 → 4]	−7.77884	0.291081	11.884

FIG. 4.   Comparison between the model data (black lines) and the fitting function in Eq. (19) for $D_q^{u+d}(Q^2)$ (dashed red). Left panel is before QCD evolution at the initial scale and right panel is after the QCD evolution at $\mu^2 = 4$ GeV^2 evolved from $\mu_0^2 = 0.32$ GeV^2 and $\mu_0^2 = 1.00$ GeV^2, respectively. The solid lines represent the actual model results, while the dashed lines correspond to the fits using Eq. (19) with the parameters given in Table I.

bands in our results are due to a 2% uncertainty in the model parameters. The uncertainty in the $D_q(Q^2)$ reflects that the form factor is highly sensitive to our model parameters. The actual uncertainty of the model parametrization in the low Q^2 region, $0.01 \leq Q^2 \leq 0.1$ GeV^2, is shown in Fig. 3.

It turns out that the form factor $D^{u+d}(Q^2)$ can be sufficiently described by the following multipole function defined as

$$D_{\mathrm{fit}}^q(Q^2) = 4C_{\mathrm{fit}}^q(Q^2) = \frac{a_q}{(1 + b_q Q^2)^{c_q}}, \qquad (19)$$
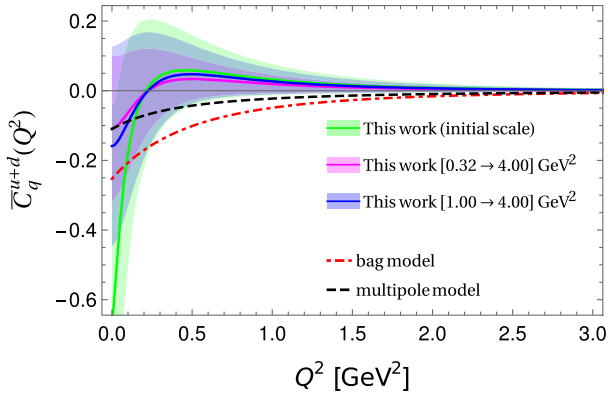

FIG. 5.   The GFF $\bar{C}_q^{u+d}(Q^2)$ as a function of Q^2. The dashed green lines with green bands are the results at the initial scale, while the solid magenta lines with magenta bands and the dash-dotted blue lines with purple bands represent the results at $\mu^2 = 4$ GeV^2 evolved from the initial scale $\mu_0^2 = 0.32$ GeV^2 and $\mu_0^2 = 1.00$ GeV^2, respectively. The error bands correspond to 2% uncertainty in the model parameters. Our results are compared with the bag model [26] (dash-dotted red) and the multipole model [2] (dashed black).

where the parameters a_q, b_q, and c_q are given in the Table I. In Fig. 4, we compare the model data of the D-term form factor and the multipole function given in Eq. (19). The form factor $\bar{C}(Q^2)$ in the quark-diquark model is illustrated in Fig. 5. In accord with the bag model [26] and the multipole model [2], $\bar{C}(Q^2)$ in the present model is negative at low Q^2 (<0.22 GeV^2); however, we observe a distinctly different behavior in the region of $Q^2 > 0.22$ GeV^2, where it exhibits positive distribution, while in other models $\bar{C}(Q^2)$ is always negative. The positive distribution decreases with QCD evolution. We remark that the D-term and $\bar{C}(Q^2)$ form factors presented in Figs. 2, 3, and 5, respectively, directly follow from Eqs. (13) and (14) computed using the model wave functions and are not the results of any independent parametrization.

We present a comparison of the GFFs at $Q^2 = 0$ with those of the various phenomenological models, lattice QCD and existing experimental data for $D_q(0)$ in Table II. For the $A_q(0)$ and $J_q(0)$ form factors, our estimation is in more or less agreement with the predictions of Refs. [2,14,15,37–41] at renormalization scale of $\mu^2 = 4$ GeV^2. The QCD sum rule (QCDSR) (I and II) gives a higher value of $A_q(0)$, since the scale is relatively low $\mu^2 = 1$ GeV^2 [8]. Note that in the χQSM and Skyrme models, there are only quarks and antiquarks to carry the nucleon's angular momentum and they must carry 100% of it, and thus $2J_q(0) = A_q(0) = 1$. The results in AdS/ QCD models are presented at model scale, where u and d quarks together carry $\sim$90% of nucleon momentum. For the form factor $D_q(0)$, our extrapolated value is overestimated when we compare it with lattice QCD results [15,37,38] and the predictions of Refs. [7,8,74] as well as the experimental data from JLab [3] but they differ from the other predictions presented in the Table II. Our predictions for $\bar{C}_q(0)$ accords with IFF [2] and the

TABLE II.   The GFFs of valence quark combination at $Q^2 = 0$ compared with other predictions and JLab data. The Skyrme and χQSM models predictions have been obtained by considering both the quark and the gluon contributions and these are scale independent. Here, $(\mu_0 \to \mu)$ represents the evolution from the initial scale μ_0 to the final scale μ.

Approaches/Models	$A_q^{u+d}(0)$	$J_q(0) = \frac{1}{2}[A_q^{u+d}(0) + B_q^{u+d}(0)]$	$D_{\text{fit}}^{u+d}(0) = 4C_{\text{fit}}^{u+d}(0)$	$\bar{C}_q^{u+d}(0)$
This work ($\sqrt{0.32}$ GeV $\to$ 2 GeV)	0.593	0.269	-5.586	-0.109
This work (1.00 GeV $\to$ 2 GeV)	0.825	0.369	-7.778	-0.159
LQCD (2 GeV) [14]	0.675	0.34	$\cdots$	$\cdots$
LQCD (2 GeV) [15]	0.547	0.33	-0.80	$\cdots$
LQCD (2 GeV) [37]	0.553	0.238	-1.02	$\cdots$
LQCD (2 GeV) [38]	0.520	0.213	-1.07	$\cdots$
LQCD (2 GeV) [39]	0.572	0.226	$\cdots$	$\cdots$
LQCD (2 GeV) [40]	0.565	0.314	$\cdots$	$\cdots$
χPT (2 GeV) [41]	0.538	0.24	-1.44	$\cdots$
IFF (2 GeV) [2]	0.55	0.24	-1.28	-0.11
Asymptotic (∞GeV) [24]	$\cdots$	0.18	$\cdots$	-0.15
QCDSR-I (1 GeV) [8]	0.79	0.36	-1.832	-2.1×10^{-2}
QCDSR-II (1 GeV) [8]	0.74	0.30	-1.64	-2.5×10^{-2}
Skyrme [10]	1	0.5	-3.584	$\cdots$
Skyrme [11]	1	0.5	-2.832	$\cdots$
χQSM [7]	1	0.5	-1.88	$\cdots$
χQSM [9]	1	0.5	-4.024	$\cdots$
χQSM [44]	$\cdots$	$\cdots$	-3.88	$\cdots$
AdS/QCD Model I [6]	0.917	0.415	$\cdots$	$\cdots$
AdS/QCD Model II [6]	0.8742	0.392	$\cdots$	$\cdots$
LCSR-LO [4]	$\cdots$	$\cdots$	-2.104	$\cdots$
KM15 fit [74]	$\cdots$	$\cdots$	-1.744	$\cdots$
DR [16]	$\cdots$	$\cdots$	-1.36	$\cdots$
JLab data [3]	$\cdots$	$\cdots$	-1.688	$\cdots$
IP [17]	$\cdots$	$\cdots$	$\cdots$	1.4×10^{-2}

TABLE III.   The mechanical properties: pressure, energy density, and mechanical radius of nucleon.

Approaches/Models	p_0 [GeV/fm^3]	$\mathcal{E}$ [GeV/fm^3]	$\langle r_{\text{mech}}^2 \rangle$ [fm^2]
This work ($\sqrt{0.32}$ GeV $\to$ 2 GeV)	0.29	3.21	0.74
This work (1.00 GeV $\to$ 2 GeV)	0.40	4.58	0.74
QCDSR set-I (1 GeV) [8]	0.67	1.76	0.54
QCDSR set-II (1 GeV) [8]	0.62	1.74	0.52
Skyrme model [10]	0.47	2.28	$\cdots$
modified Skyrme model [11]	0.26	1.445	$\cdots$
χQSM [7]	0.23	1.70	$\cdots$
Soliton model [9]	0.58	3.56	$\cdots$
LCSM-LO [4]	0.84	0.92	0.54

asymptotical value at three loops level reported in Ref. [24], however, substantially differ from the predictions of QCDSR [8] and IP [17]. Note that the intrinsic spin sum rule for a transversely polarized nucleon not only involves the form factors A_q and B_q but also $\bar{C}_q$ [24,63,75,76].

IV. MECHANICAL PROPERTIES

The pressure and the energy density in the center of nucleon are directly related to the GFFs as [1]

$$p_0 = -\frac{1}{24\pi^2 M_n} \int_0^\infty dQ^2 Q^3 D(Q^2),$$

$$\mathcal{E} = \frac{M_n}{4\pi^2} \int_0^\infty dQ^2 \left(A(Q^2) + \frac{Q^2}{4M_n^2} D(Q^2) \right), \quad (20)$$

respectively, while the mechanical radius can be obtained by

$$\langle r_{\text{mech}}^2 \rangle = 6 D_{\text{fit}}(0) \left[\int_0^\infty dQ^2 D(Q^2) \right]^{-1}. \quad (21)$$

Here, M_n denotes the mass of nucleon. We compute the pressure, energy densities in the proton and the mechanical radius using the GFFs evaluated in the quark-diquark model. Our results on the mechanical quantities p_0, $\mathcal{E}$, and $\langle r^2_{\text{mech}} \rangle$ of the proton compared to other existing theoretical predictions are shown in the Table III. It can be seen from Table III that our prediction on the p_0 is underestimated but comparable with χQSM model [7] and the modified Skyrme model [11]. Note that the available theoretical predictions differ considerably from each other. Our results on $\mathcal{E}$ in quark-diquark model is close to the predictions of the soliton model [9], but overestimated compared to the other presented predictions [7–11]. However, different approaches/models demonstrate considerable deviations from each other while predicting $\mathcal{E}$. Meanwhile, our predictions on the mechanical radius, $\langle r^2_{\text{mech}} \rangle$, are larger than the prediction of Refs. [4,8].

A. Pressure and shear force distributions

The distributions of pressure and shear forces inside the nucleon are given by

$$p(b) = \frac{1}{6M_n} \frac{1}{b^2} \frac{d}{db} b^2 \frac{d}{db} \tilde{D}(b),$$

$$s(b) = -\frac{1}{4M_n} b \frac{d}{db} \frac{1}{b} \frac{d}{db} \tilde{D}(b), \qquad (22)$$

where

$$\tilde{D}(b) = \int \frac{d^2 \vec{q}_\perp}{(2\pi)^2} e^{i\vec{q}_\perp \cdot \vec{b}_\perp} D(Q^2). \qquad (23)$$

Here, $b = |\vec{b}_\perp|$ represents the impact parameter. The pressure distribution $p(b)$ must satisfy the stability condition, also known as the von Laue condition [77],

$$\int_0^\infty db\, b^2 p(b) = 0. \qquad (24)$$

This is a consequence of the energy momentum tensor conservation and allows us to understand how the internal forces balance inside a composed system [1,18]. We illustrate the distribution $b^2 p(b)$ as a function of b in Fig. 6(a). We compare our result with the distribution evaluated in leading order light-cone sum rule [4] and the distribution obtained from the fitting functions of the experimental data for $D(Q^2)$ at JLab [3]. The distribution must have at least one node to comply with the von Laue condition, Eq. (24). It can be noticed that the distribution has a positive core and a negative tail. This pattern ensures the mechanical stability arguments: the repulsive forces are required in the inner domain to prevent collapse and the attractive forces in the outer region to bind the system. Our pressure distribution crosses the zero-line (zero-crossing) near 0.9 fm (central line), whereas this zero-crossing appears at 0.7 fm in the result based on light-cone sum rule [4] and near 0.6 fm in the JLab distribution [3]. Overall, the qualitative behavior of the pressure distribution evaluated in the quark-diquark model is found to be in agreement with the experimental observation [3] as well as other theoretical predictions [4,7,9–12]. The shear force distribution, $b^2 s(b)$ has been displayed in Fig. 6(b). $s(b)$ has a connection to surface tension and surface energy, which are positive in stable hydrostatic systems [1]. We find that $s(b)$ (central line) is positive in all region of b. The positivity of this distribution was observed in all studies so far. We again notice that the qualitative nature of our result is in accordance with other approaches [4,7,9–12].

On the other hand, the spherical shell of radius b in the nucleon experiences the normal and tangential forces: F_n and F_t, respectively, which are defined as [4]
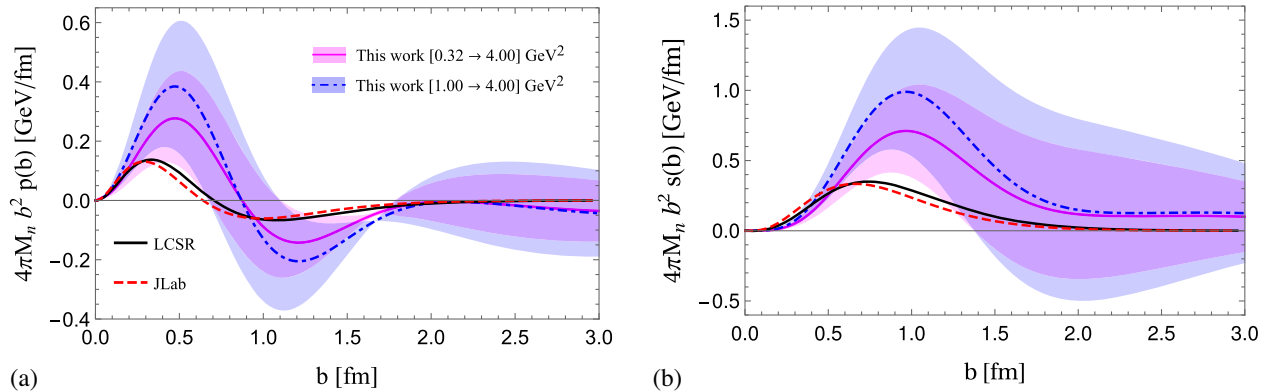

(a)

(b)

FIG. 6. Plots of (a) the pressure distribution $4\pi M_n b^2 p(b)$, and (b) the shear force distribution $4\pi M_n b^2 s(b)$ as a function of b. Our results are compared with results based on LCSR evaluated in Ref. [4] (black line) and using the fitting function of $D(Q^2)$ based on experimental data [3] (red dashed line). The solid magenta lines with magenta bands and the dash-dotted blue lines with purple bands represent the results at $\mu^2 = 4$ GeV^2 evolved from the initial scale $\mu_0^2 = 0.32$ GeV^2 and $\mu_0^2 = 1.00$ GeV^2, respectively.
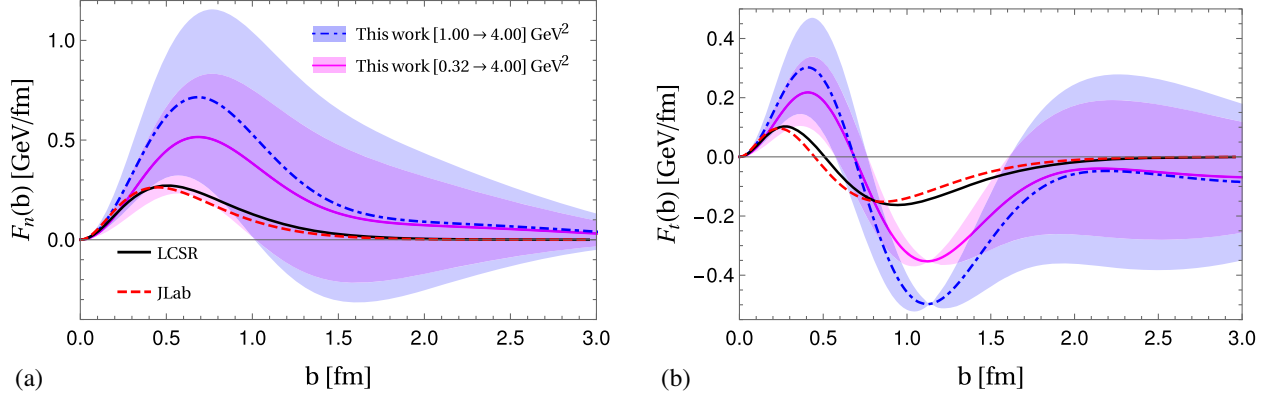
FIG. 7.   Plots of (a) the normal forces F_n, and (b) the tangential forces F_t as a function of b. Our results are compared with results based on LCSR evaluated in Ref. [4] (black line) and using the fitting function of $D(Q^2)$ based on experimental data [3] (red dashed line). The solid magenta lines with magenta bands and the dash-dotted blue lines with purple bands represent the results at $\mu^2 = 4$ GeV^2 evolved from the initial scale $\mu_0^2 = 0.32$ GeV^2 and $\mu_0^2 = 1.00$ GeV^2, respectively.

$$F_n(b) = 4\pi M_n b^2 \left(p(b) + \frac{2}{3} s(b) \right),$$

$$F_t(b) = 4\pi M_n b^2 \left(p(b) - \frac{1}{3} s(b) \right). \qquad (25)$$

We show the estimated normal and tangential forces for the valence quark combination in Fig 7(a) and Fig 7(b), respectively. One notices that $F_n(b)$ is always positive, whereas $F_t(b)$ has a positive core (repulsive force) surrounded by a negative tail (attractive force) with a zero-crossing near $b \sim 0.7$ fm. The repulsive force has the peak near $b \sim 0.4$ fm, and the maximum of the negative force that is responsible for the binding occurs near $b \sim 1.1$ fm. However, the binding force is stronger than the repulsive force. The qualitative behavior of the forces in the quark-diquark model is fairly consistent with the light-cone sum rule [4], estimated distribution from JLab fitting function for $D(Q^2)$ [3], and chiral quark-soliton [7] model as well.

We also compute the two-dimensional Galilean energy density, radial pressure, tangential pressure, isotropic pressure, and pressure anisotropy, which in Drell-Yan-West frame are defined as [2]

$$\mu_a(b) = M_n \left\{ \frac{A_a(b)}{2} + \bar{C}_a(b) \right.$$
$$\left. + \frac{1}{4M_n^2} \frac{1}{b} \frac{d}{db} \left(b \frac{d}{db} \left[\frac{B_a(b)}{2} - 4C_a(b) \right] \right) \right\}$$

$$\sigma_{r,a}(b) = M_n \left\{ -\bar{C}_a(b) + \frac{1}{M_n^2} \frac{1}{b} \frac{dC_a(b)}{db} \right\}$$

$$\sigma_{t,a}(b) = M_n \left\{ -\bar{C}_a(b) + \frac{1}{M_n^2} \frac{d^2 C_a(b)}{db^2} \right\}$$

$$\sigma_a(b) = M_n \left\{ -\bar{C}_a(b) + \frac{1}{2} \frac{1}{M_n^2} \frac{1}{b} \frac{d}{db} \left(b \frac{dC_a(b)}{db} \right) \right\}$$

$$\Pi_a(b) = M_n \left\{ -\frac{1}{M_n^2} b \frac{d}{db} \left(b \frac{dC_a(b)}{db} \right) \right\}, \qquad (26)$$
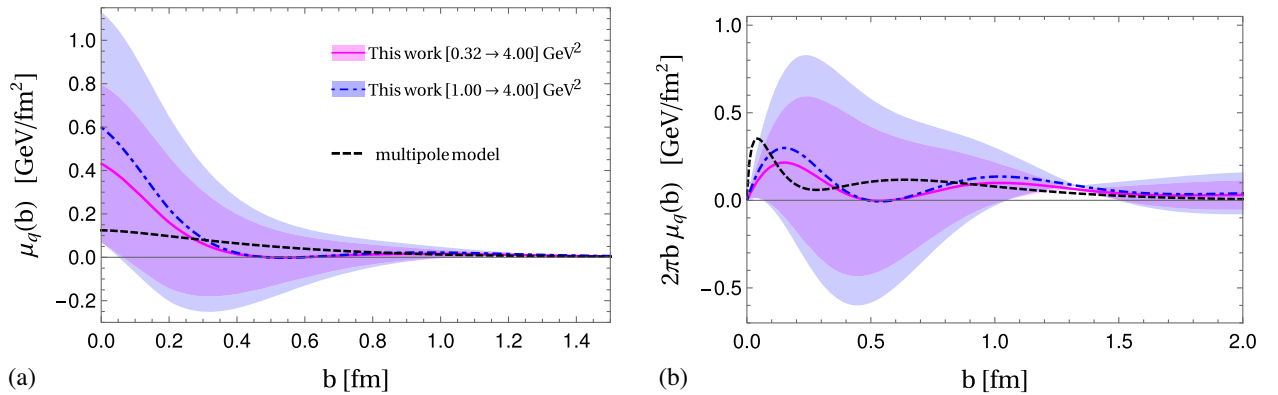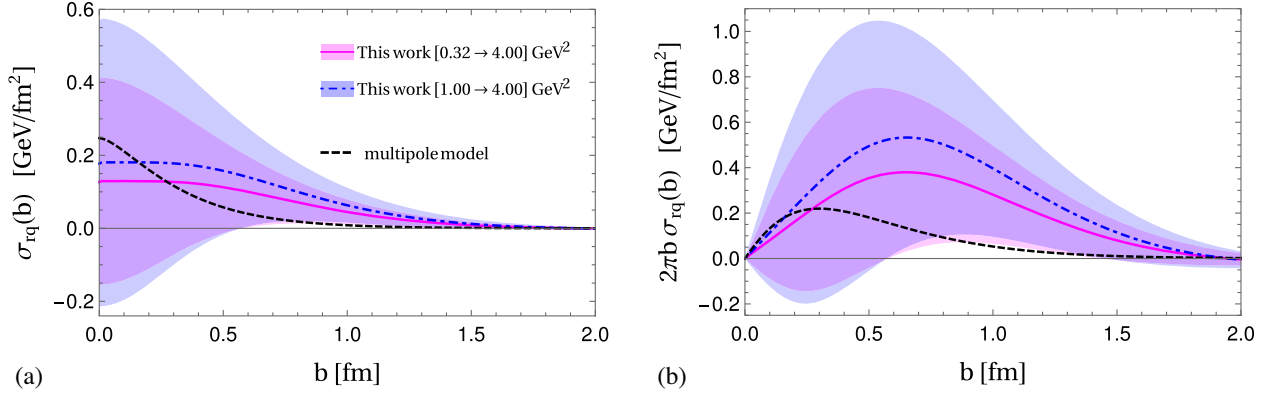

FIG. 8.   Plots of the two-dimensional Galilean energy density (a) $\mu_q(b)$, and (b) $2\pi b \mu_q(b)$. The solid magenta lines with magenta bands and the dash-dotted blue lines with purple bands represent the results at $\mu^2 = 4$ GeV^2 evolved from the initial scale $\mu_0^2 = 0.32$ GeV^2 and $\mu_0^2 = 1.00$ GeV^2, respectively. Our results are compared with the results in a multipole model (black dashed line) [2].
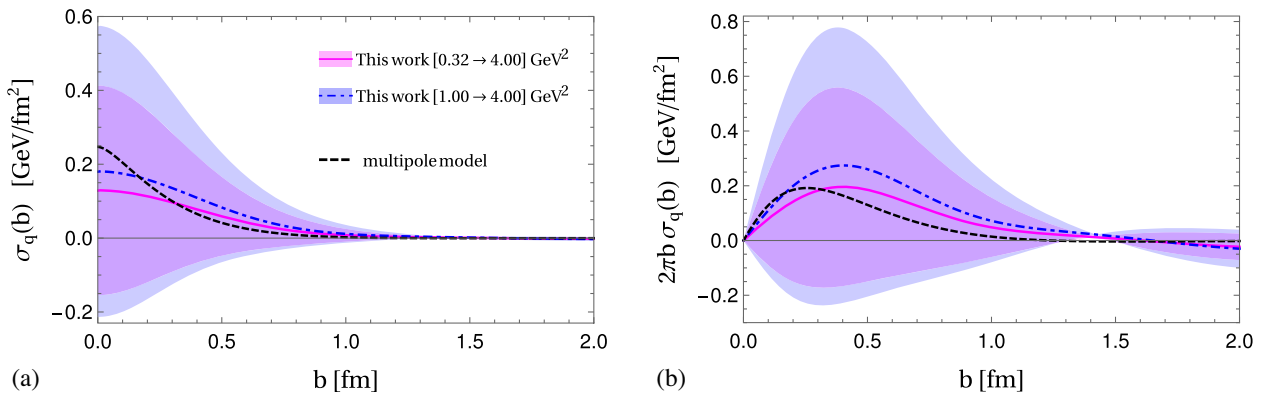
FIG. 9.   Plots of the two-dimensional radial pressure (a) $\sigma_{r,q}(b)$, and (b) $2\pi b \sigma_{r,q}(b)$. The legends are same as mentioned in Fig. 8.
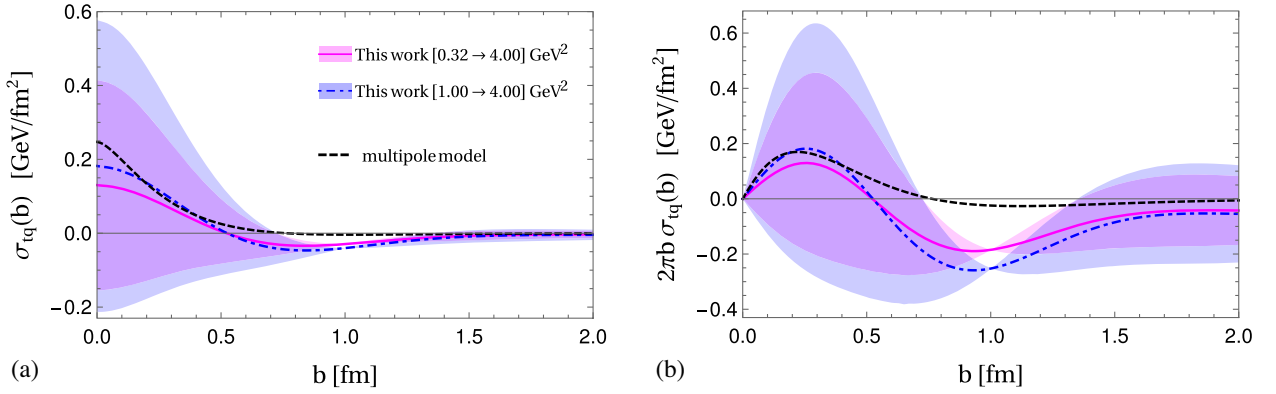
FIG. 10.   Plots of the two-dimensional tangential pressure (a) $\sigma_{t,q}(b)$, and (b) $2\pi b \sigma_{t,q}(b)$. The legends are same as mentioned in Fig. 8.

respectively, where the form factors in position space are given by their Fourier transform:

$$\chi(b) = \int \frac{d^2\vec{q}_\perp}{(2\pi)^2} e^{i\vec{q}_\perp \cdot \vec{b}_\perp} \chi(q^2). \qquad (27)$$

The distributions defined in Eq. (26) are illustrated in Figs 8, 9, 10, 11, and 12. We observe that the energy density $\mu_q(b)$ in Fig. 8 and the radial pressure $\sigma_{r,q}(b)$ in

Fig. 9 are always positive having the peaks at center of the proton ($b = 0$). On the other hand, in Fig. 10, the tangential pressure $\sigma_{t,q}(b)$ is positive at low b with maxima at the center but it shows negative distribution when $b > 0.55$ fm. The isotopic pressure $\sigma_q(b)$ in Fig. 11 exhibits a similar behavior as the radial pressure; however, it also shows a slightly negative distribution at large b (>1.7 fm). The pressure anisotropy in Fig. 12 vanishes at the center of the proton, as required by spherical symmetry, and is positive

FIG. 11.   Plots of the two-dimensional isotopic pressure (a) $\sigma_q(b)$, and (b) $2\pi b \sigma_q(b)$. The legends are same as mentioned in Fig. 8.
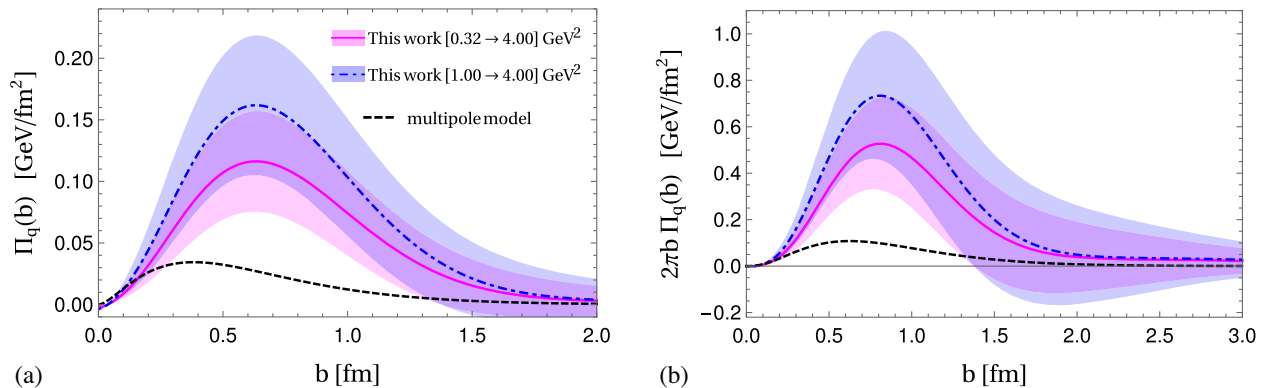
FIG. 12.   Plots of the two-dimensional pressure anisotropy (a) $\Pi_q(b)$, and (b) $2\pi b\Pi\sigma_q(b)$. The legends are same as mentioned in Fig. 8.

anywhere else, indicating that the radial pressure is always larger than the tangential one. Our predictions on the energy density, radial pressure, tangential pressure, isotropic pressure, and pressure anisotropy are compared with the results in a simple multipole model [2]. The qualitative behavior of those distributions in Figs. 8–12, within the error bands, are found be consistent with the multipole model reported in Ref. [2]. We have also observed that the qualitative behavior remains the same going from $\mu_0^2 = 0.32$ GeV^2 to $\mu_0^2 = 1.0$ GeV^2.

V. SUMMARY

Gravitational form factors provide us with knowledge on different aspects of the nucleon's structure, e.g., the pressure and energy distributions, the distribution and stabilization of the strong force inside the nucleon as well as quantities related to its geometric shape. One can also get the information on the fractions of the longitudinal momenta carried by the constituents and the total angular momentum from the GFFs. In this paper, we have evaluated the GFFs of the proton in a light-front quark-diquark model with AdS/QCD predicted wave functions. We have showed explicit Q^2 behavior of the gravitational form factors in this model and observed that the GFFs $A(Q^2)$ and $B(Q^2)$ are comparable with lattice QCD results [38]. We have found that the GFF $D(Q^2)$ of proton can be described by a multipole fit function. We have observed that the qualitative nature of $D(Q^2)$ in the quark-diquark model is in accord with the experimental data extracted from DVCS process at JLab [3] and lattice QCD predictions [38]. We have compared the values of the GFFs at $Q^2 = 0$ with the existing theoretical predictions and the data from JLab. Our results on $A_q(0)$ and $J_q(0)$ were found to be in fair agreement with the lattice QCD and chiral perturbation theory predictions. Meanwhile, our prediction on $D^q(0)$ appeared to be larger while comparing with the JLab data as well as the available theoretical predictions. It should also be noted that there are large discrepancies among the theoretical predictions on the $D_q(0)$. We have extracted

the value of $\bar{C}_q(0)$ which is comparable with that in Refs. [2,24] but larger than those values reported in Refs. [8,17].

We have employed the GFFs to evaluate the pressure and energy density distributions inside the proton as well as the mechanical radius of the proton and compared them with the existing theoretical predictions. We have observed that the pressure in the center of the proton p_0 in quark-diquark model is underestimated with respect to QCDSR [8], LCSR-LO [4], Soliton model [9] and Skyrme model [10] but close to that in χQSM [7] and modified Skyrme model [11], while our prediction on the energy density $\mathcal{E}$ is close to that in the soliton model [9]. However, there are large discrepancies among the theoretical predictions on p_0 and $\mathcal{E}$. Mechanical radius, $\langle r_{\text{mech}}^2 \rangle$, has been found to be somewhat larger compared to the existing predictions provided by LCSR-LO [4] and QCDSR [8].

We have demonstrated the pressure $p(b)$ and shear force $s(b)$ distributions inside the proton in the quark-diquark model. We have noticed that $p(b)$ has a positive core and a negative tail, while $s(b)$ is always positive which is consistent with the experimental observation and other theoretical predictions. On the other hand, we also found that the normal force $F_n(b)$ is always repulsive but the tangential force $F_t(b)$ is repulsive near the center but attractive for $b > 0.5$ fm. These behaviors are again in fair agreement with experimental observation and other theoretical predictions. We have also computed the two-dimensional Galilean energy density, radial pressure, tangential pressure, isotropic pressure, and pressure anisotropy in this present model, which qualitatively have been found to be consistent with a multipole model.

APPENDIX A: MATRIX ELEMENTS OF $T^{\mu\nu}$

1. Matrix elements of T^{++}

$$\langle P+q, \uparrow|T_q^{++}|P,\uparrow\rangle = 2(P^+)^2 \int \frac{d^2k_\perp dx}{16\pi^3} x[\psi_{+\frac{1}{2}}^{\uparrow *}(x,\vec{k'}_\perp)\psi_{+\frac{1}{2}}^{\uparrow}(x,\vec{k}_\perp) + \psi_{-\frac{1}{2}}^{\uparrow *}(x,\vec{k'}_\perp)\psi_{-\frac{1}{2}}^{\uparrow}(x,\vec{k}_\perp)]$$

$$= 2(P^+)^2 \int dxx\left[N_1^2 x^{2a_1}(1-x)^{2b_1+1} + N_2^2 x^{2a_2-2}(1-x)^{2b_2+3}\frac{1}{M^2}\left(\frac{\kappa^2}{\log(1/x)} - \frac{Q^2}{4}\right)\right]$$

$$\times \exp\left[-\frac{\log(1/x)}{\kappa^2}\frac{Q^2}{4}\right]$$

$$= 2(P^+)^2\mathcal{I}_1^q(Q^2), \tag{A1}$$

where $\vec{k'}_\perp = \vec{k}_\perp + (1-x)\vec{q}_\perp$. Using the matrix elements Eq. (4),

$$\langle P+q, \uparrow|T_q^{++}|P,\uparrow\rangle = 2(P^+)^2 A^q(Q^2). \tag{A2}$$

Therefore,

$$A^q(Q^2) = \mathcal{I}_1^q(Q^2). \tag{A3}$$

$$\langle P+q, \uparrow|T_q^{++}|P,\downarrow\rangle + \langle P+q, \downarrow|T_q^{++}|P,\uparrow\rangle = 2(P^+)^2 \int \frac{d^2k_\perp dx}{16\pi^3} x[\{\psi_{+\frac{1}{2}}^{\uparrow *}(x,\vec{k'}_\perp)\psi_{+\frac{1}{2}}^{\downarrow}(x,\vec{k}_\perp) + \psi_{-\frac{1}{2}}^{\uparrow *}(x,\vec{k'}_\perp)\psi_{-\frac{1}{2}}^{\downarrow}(x,\vec{k}_\perp)\}$$

$$+ \{\psi_{+\frac{1}{2}}^{\downarrow *}(x,\vec{k'}_\perp)\psi_{+\frac{1}{2}}^{\uparrow}(x,\vec{k}_\perp) + \psi_{-\frac{1}{2}}^{\downarrow *}(x,\vec{k'}_\perp)\psi_{-\frac{1}{2}}^{\uparrow}(x,\vec{k}_\perp)\}]$$

$$= 2(P^+)^2(iq_\perp^2)2\int dxN_1 N_2 \frac{1}{M_n} x^{a_1+a_2}(1-x)^{b_1+b_2+2}\exp\left[-\frac{\log(1/x)}{\kappa^2}\frac{Q^2}{4}\right]$$

$$= \frac{2(P^+)^2}{M_n}(iq_\perp^2)\mathcal{I}_2^q(Q^2). \tag{A4}$$

Using the matrix elements Eq. (4),

$$\langle P+q, \uparrow|T_q^{++}|P,\downarrow\rangle + \langle P+q, \downarrow|T_q^{++}|P,\uparrow\rangle = B(Q^2)\frac{2(P^+)^2}{M}(iq_\perp^2). \tag{A5}$$

Therefore,

$$B^q(Q^2) = \mathcal{I}_2^q(Q^2). \tag{A6}$$

APPENDIX B: T^{+-}: UP GOING TO DOWN PLUS DOWN GOING TO UP MATRIX ELEMENTS

$$
\begin{aligned}
\langle P+q, \uparrow|T_q^{+-}|P,\downarrow\rangle + \langle P+q,\downarrow|T_q^{+-}|P,\uparrow\rangle &= \int \frac{d^2k_\perp dx}{16\pi^3}\frac{(k_\perp^2+m^2)}{x}[\{\psi_{+\frac{1}{2}}^{\uparrow*}(x,\vec{k'}_\perp)\psi_{+\frac{1}{2}}^{\downarrow}(x,\vec{k}_\perp) + \psi_{-\frac{1}{2}}^{\uparrow*}(x,\vec{k'}_\perp)\psi_{-\frac{1}{2}}^{\downarrow}(x,\vec{k}_\perp)\}\\
&\quad + \{\psi_{+\frac{1}{2}}^{\downarrow*}(x,\vec{k'}_\perp)\psi_{+\frac{1}{2}}^{\uparrow}(x,\vec{k}_\perp) + \psi_{-\frac{1}{2}}^{\downarrow*}(x,\vec{k'}_\perp)\psi_{-\frac{1}{2}}^{\uparrow}(x,\vec{k}_\perp)\}]\\
&= 2(iq_\perp^2)\int dx N_1 N_2 \frac{1}{M_n}x^{a_1+a_2-2}(1-x)^{b_1+b_2+2}\\
&\quad \times \left[\frac{\kappa^2(1-x)^2}{\log(1/x)} + \frac{Q^2(1-x)^2}{4} + m^2\right]\exp\left[-\frac{\log(1/x)}{\kappa^2}\frac{Q^2}{4}\right]\\
&= \frac{(iq_\perp^2)}{M}\mathcal{I}_4^q(Q^2).
\end{aligned}
\tag{B1}
$$

Here m is the quark mass which is zero in the present model. Using the matrix elements Eq. (4),

$$
\langle P+q, \uparrow|T_q^{+-}|P,\downarrow\rangle + \langle P+q,\downarrow|T_q^{+-}|P,\uparrow\rangle = \left[A(Q^2)(2M) - B(Q^2)\frac{Q^2}{M} + C(Q^2)\frac{4Q^2}{M} + \bar{C}(Q^2)(4M)\right](-iq_\perp^2). \tag{B2}
$$

Therefore,

$$
\left[A(Q^2)(2M) - B(Q^2)\frac{Q^2}{M} + C(Q^2)\frac{4Q^2}{M} + \bar{C}(Q^2)(4M)\right] = \frac{\mathcal{I}_4^q(Q^2)}{M}. \tag{B3}
$$

APPENDIX C: T^{-2}: UP GOING TO DOWN PLUS DOWN GOING TO UP MATRIX ELEMENTS

$$
\begin{aligned}
\langle P+q, \uparrow|T_q^{-2}|P,\downarrow\rangle + \langle P+q,\downarrow|T_q^{-2}|P,\uparrow\rangle &= -\frac{4}{P^+}\int\frac{d^2k_\perp dx}{16\pi^3}\left(\frac{k_2^\perp(-(k_1^\perp)^2+(k_2^\perp)^2+m^2)}{x(1-x)}\right)[\psi_{+\frac{1}{2}}^{\uparrow*}(x,k'_\perp)\psi_{+\frac{1}{2}}^{\downarrow}(x,k_\perp)\\
&\quad + \psi_{-\frac{1}{2}}^{\uparrow*}(x,k'_\perp)\psi_{-\frac{1}{2}}^{\downarrow}(x,k_\perp) + \psi_{+\frac{1}{2}}^{\downarrow*}(x,k'_\perp)\psi_{+\frac{1}{2}}^{\uparrow}(x,k_\perp) + \psi_{-\frac{1}{2}}^{\downarrow*}(x,k'_\perp)\psi_{-\frac{1}{2}}^{\uparrow}(x,k_\perp)]\\
&= -\frac{1}{P^+}i(q_\perp^2)^2\int dx N_1 N_2 \frac{1}{M}x^{a_1+a_2-2}(1-x)^{b_1+b_2+2}\left(\frac{1}{x}\right)^{-\frac{Q^2}{4\kappa^2}}\\
&\quad \times\left(\frac{4(x-1)^2\kappa^2}{\log(1/x)} + (Q^2(x-1)^2 - 4m^2)\right)\\
&= -\frac{1}{P^+}\frac{i(q_\perp^2)^2}{2M}\mathcal{I}_3^q(Q^2).
\end{aligned}
\tag{C1}
$$

Using the matrix elements Eq. (4),

$$
\langle P+q, \uparrow|T_q^{-2}|P,\downarrow\rangle + \langle P+q,\downarrow|T_q^{-2}|P,\uparrow\rangle = -\frac{1}{P^+}\frac{i(q_\perp^2)^2}{2M}[2A(Q^2)M^2 - (B(Q^2)-4C(Q^2))Q^2]. \tag{C2}
$$

Therefore,

$$
2A(Q^2)M^2 - (B(Q^2) - 4C(Q^2))Q^2 = \mathcal{I}_3^q(Q^2). \tag{C3}
$$

APPENDIX D: T^{-1}: UP GOING TO DOWN PLUS DOWN GOING TO UP MATRIX ELEMENTS

$$
\begin{aligned}
\langle P+q, \uparrow|T_q^{-1}|P, \downarrow\rangle + \langle P+q, \downarrow|T_q^{-1}|P, \uparrow\rangle &= -\frac{4}{P^+}\int \frac{d^2k_\perp dx}{16\pi^3}\left(\frac{k_1^\perp(-(k_1^\perp)^2+(k_2^\perp)^2+m^2)}{x(1-x)}\right)[\psi_{+\frac{1}{2}}^{\uparrow*}(x,k'_\perp)\psi_{+\frac{1}{2}}^{\downarrow}(x,k_\perp) \\
&\quad + \psi_{-\frac{1}{2}}^{\uparrow*}(x,k'_\perp)\psi_{-\frac{1}{2}}^{\downarrow}(x,k_\perp) + \psi_{+\frac{1}{2}}^{\downarrow*}(x,k'_\perp)\psi_{+\frac{1}{2}}^{\uparrow}(x,k_\perp) + \psi_{-\frac{1}{2}}^{\downarrow*}(x,k'_\perp)\psi_{-\frac{1}{2}}^{\uparrow}(x,k_\perp)] \\
&= -\frac{1}{P^+}iq_\perp^1 q_\perp^2 \int dx N_1 N_2 \frac{1}{M}x^{a_1+a_2-2}(1-x)^{b_1+b_2+2}\left(\frac{1}{x}\right)^{-\frac{Q^2}{4\kappa^2}} \\
&\quad \times \left(\frac{4(x-1)^2\kappa^2}{\log(1/x)} + (Q^2(x-1)^2-4m^2)\right) \\
&= -\frac{1}{P^+}\frac{iq_\perp^1 q_\perp^2}{2M}\mathcal{I}_5^q(Q^2).
\end{aligned}
\tag{D1}
$$

Using the matrix elements Eq. (4),

$$
\langle P+q, \uparrow|T_q^{-1}|P, \downarrow\rangle + \langle P+q, \downarrow|T_q^{-1}|P, \uparrow\rangle = -\frac{1}{P^+}\frac{iq_\perp^1 q_\perp^2}{2M}[2A(Q^2)M^2-(B(Q^2)-4C(Q^2))Q^2].
\tag{D2}
$$

Therefore,

$$
2A(Q^2)M_n^2 - (B(Q^2)-4C(Q^2))Q^2 = \mathcal{I}_5^q(Q^2) = \mathcal{I}_3^q(Q^2).
\tag{D3}
$$

---

[1] M. V. Polyakov and P. Schweitzer, Int. J. Mod. Phys. A **33,** 1830025 (2018).

[2] C. Lorcé, H. Moutarde, and A. P. Trawiński, Eur. Phys. J. C **79,** 89 (2019).

[3] V. Burkert, L. Elouadrhiri, and F. Girod, Nature (London) **557,** 396 (2018).

[4] I. Anikin, Phys. Rev. D **99,** 094026 (2019).

[5] K. A. Mamo and I. Zahed, Phys. Rev. D **101,** 086003 (2020).

[6] C. Mondal, Eur. Phys. J. C **76,** 74 (2016).

[7] K. Goeke, J. Grabis, J. Ossmann, M. V. Polyakov, P. Schweitzer, A. Silva, and D. Urbano, Phys. Rev. D **75,** 094021 (2007).

[8] K. Azizi and U. Özdem, Eur. Phys. J. C **80,** 104 (2020).

[9] J. H. Jung, U. Yakhshiev, H. C. Kim, and P. Schweitzer, Phys. Rev. D **89,** 114021 (2014).

[10] C. Cebulla, K. Goeke, J. Ossmann, and P. Schweitzer, Nucl. Phys. A**794,** 87 (2007).

[11] H. C. Kim, P. Schweitzer, and U. Yakhshiev, Phys. Lett. B **718,** 625 (2012).

[12] P. E. Shanahan and W. Detmold, Phys. Rev. Lett. **122,** 072003 (2019).

[13] P. E. Shanahan and W. Detmold, Phys. Rev. D **99,** 014511 (2019).

[14] P. Hägler et al. (LHPC and SESAM Collaborations), Phys. Rev. D **68,** 034505 (2003).

[15] M. Göckeler et al. (QCDSF Collaboration), Phys. Rev. Lett. **92,** 042002 (2004).

[16] B. Pasquini, M. V. Polyakov, and M. Vanderhaeghen, Phys. Lett. B **739,** 133 (2014).

[17] M. V. Polyakov and H. D. Son, J. High Energy Phys. 09 (2018) 156.

[18] M. V. Polyakov, Phys. Lett. B **555,** 57 (2003).

[19] Z. Abidin and C. E. Carlson, Phys. Rev. D **79,** 115003 (2009).

[20] M. Varma and P. Schweitzer, Phys. Rev. D **102,** 014047 (2020).

[21] M. J. Neubelt, A. Sampino, J. Hudson, K. Tezgin, and P. Schweitzer, Phys. Rev. D **101,** 034013 (2020).

[22] A. Rajan, T. Gorda, S. Liuti, and K. Yagi, arXiv:1812.01479.

[23] K. Kumerički and D. Müller, EPJ Web Conf. **112,** 01012 (2016).

[24] Y. Hatta, A. Rajan, and K. Tanaka, J. High Energy Phys. 12 (2018) 008.

[25] K. Tanaka, J. High Energy Phys. 01 (2019) 120.

[26] X. D. Ji, W. Melnitchouk, and X. Song, Phys. Rev. D **56,** 5511 (1997).

[27] X. D. Ji, Phys. Rev. Lett. **78,** 610 (1997).

[28] C. Adloff et al. (H1 Collaboration), Eur. Phys. J. C **13,** 371 (2000).

[29] C. Adloff et al. (H1 Collaboration), Phys. Lett. B **517,** 47 (2001).

[30] S. Chekanov *et al.* (ZEUS Collaboration), Phys. Lett. B **573,** 46 (2003).

[31] S. Chekanov *et al.* (ZEUS Collaboration), Phys. Lett. B **573,** 46 (2003).

[32] A. Airapetian *et al.* (HERMES Collaboration), Phys. Rev. Lett. **87,** 182001 (2001).

[33] N. d'Hose, E. Burtin, P. A. M. Guichon, and J. Marroncle, Eur. Phys. J. A **19,** 47 (2004).

[34] S. Stepanyan *et al.* (CLAS Collaboration), Phys. Rev. Lett. **87,** 182002 (2001).

[35] S. Diehl *et al.* (CLAS Collaboration), Phys. Rev. Lett. **125,** 182001 (2020).

[36] A. Accardi *et al.*, Eur. Phys. J. A **52,** 268 (2016).

[37] J. D. Bratt *et al.* (LHPC Collaboration), Phys. Rev. D **82,** 094502 (2010).

[38] P. Hagler *et al.* (LHPC Collaboration), Phys. Rev. D **77,** 094502 (2008).

[39] D. Brommel *et al.* (QCDSF-UKQCD Collaboration), Proc. Sci., LATTICE2007 (**2007**) 158 [arXiv:0710.1534].

[40] M. Deka *et al.*, Phys. Rev. D **91,** 014505 (2015).

[41] M. Dorati, T. A. Gail, and T. R. Hemmert, Nucl. Phys. **A798,** 96 (2008).

[42] J. W. Chen and X. d. Ji, Phys. Rev. Lett. **88,** 052003 (2002).

[43] A. V. Belitsky and X. Ji, Phys. Lett. B **538,** 289 (2002).

[44] M. Wakamatsu, Phys. Lett. B **648,** 181 (2007).

[45] P. Schweitzer, S. Bof, and M. Radici, Phys. Rev. D **66,** 114004 (2002).

[46] K. Goeke, J. Grabis, J. Ossmann, P. Schweitzer, A. Silva, and D. Urbano, Phys. Rev. C **75,** 055207 (2007).

[47] M. Wakamatsu and Y. Nakakoji, Phys. Rev. D **74,** 054006 (2006).

[48] S. J. Brodsky and G. F. de Téramond, Phys. Rev. D **77,** 056007 (2008).

[49] S. J. Brodsky and G. F. de Téramond, arXiv:1203.4025.

[50] T. Gutsche, V. E. Lyubovitskij, I. Schmidt, and A. Vega, Phys. Rev. D **89,** 054033 (2014); **92,** 019902(E) (2015).

[51] D. Chakrabarti and C. Mondal, Phys. Rev. D **92,** 074012 (2015).

[52] C. Mondal, Eur. Phys. J. C **77,** 640 (2017).

[53] D. Chakrabarti, C. Mondal, and A. Mukherjee, Phys. Rev. D **91,** 114026 (2015).

[54] D. Chakrabarti, T. Maji, C. Mondal, and A. Mukherjee, Eur. Phys. J. C **76,** 409 (2016).

[55] C. Mondal and D. Chakrabarti, Eur. Phys. J. C **75,** 261 (2015).

[56] T. Gutsche, V. E. Lyubovitskij, and I. Schmidt, Eur. Phys. J. C **77,** 86 (2017).

[57] C. Mondal, N. Kumar, H. Dahiya, and D. Chakrabarti, Phys. Rev. D **94,** 074028 (2016).

[58] T. Maji, C. Mondal, D. Chakrabarti, and O. V. Teryaev, J. High Energy Phys. 01 (2016) 165.

[59] G. F. de Téramond *et al.* (HLFHS Collaboration), Phys. Rev. Lett. **120,** 182001 (2018).

[60] T. Liu, R. S. Sufian, G. F. de Téramond, H. G. Dosch, S. J. Brodsky, and A. Deur, Phys. Rev. Lett. **124,** 082003 (2020).

[61] D. Chakrabarti and C. Mondal, Phys. Rev. D **88,** 073006 (2013).

[62] D. Chakrabarti and C. Mondal, Eur. Phys. J. C **73,** 2671 (2013).

[63] A. Harindranath, R. Kundu, and A. Mukherjee, Phys. Lett. B **728,** 63 (2014).

[64] X. Ji, X. Xiong, and F. Yuan, Phys. Lett. B **717,** 214 (2012).

[65] Z. Abidin and C. E. Carlson, Phys. Rev. D **78,** 071502 (2008).

[66] O. V. Selyugin and O. V. Teryaev, Phys. Rev. D **79,** 033003 (2009).

[67] N. Kumar, C. Mondal, and N. Sharma, Eur. Phys. J. A **53,** 237 (2017).

[68] S. Kumano, Q. T. Song, and O. V. Teryaev, Phys. Rev. D **97,** 014020 (2018).

[69] N. Kaur, N. Kumar, C. Mondal, and H. Dahiya, Nucl. Phys. **B934,** 80 (2018).

[70] Y. L. Dokshitzer, Zh. Eksp. Teor. Fiz. **73,** 1216 (1977) [Sov. Phys. JETP **46,** 641 (1977)], http://old.inspirehep.net/record/12615.

[71] V. N. Gribov and L. N. Lipatov, Sov. J. Nucl. Phys. **15,** 438 (1972), http://old.inspirehep.net/record/73449.

[72] G. Altarelli and G. Parisi, Nucl. Phys. **B126,** 298 (1977).

[73] G. P. Salam and J. Rojo, Comput. Phys. Commun. **180,** 120 (2009).

[74] I. V. Anikin *et al.*, Acta Phys. Pol. B **49,** 741 (2018).

[75] E. Leader and C. Lorce, Phys. Rev. Lett. **111,** 039101 (2013).

[76] A. Harindranath, R. Kundu, A. Mukherjee, and R. Ratabole, Phys. Rev. Lett. **111,** 039102 (2013).

[77] M. V. Lane, Ann. Phys. (Leipzig) **3–90,** 524 (1911).